Cold Crystallization of Poly(9,9-di-*n*-octyl-2,7-fluorene)

S. H. Chen,*,† Y. H. Wu,† C. H. Su,‡ U. Jeng,§ C. C. Hsieh,‡ A. C. Su,*,‡,‖ and S. A. Chen‖

Department of Materials Science and Engineering, National Dong Hwa University, Hualien 974, Taiwan; Institute of Materials Science & Engineering and Center for Nanoscience & Nanotechnology, National Sun Yat-sen University, Kaohsiung 804, Taiwan; National Synchrotron Radiation Research Center, Hsinchu 300, Taiwan; and Department of Chemical Engineering, National Tsing Hua University, Hsinchu 300, Taiwan

Received January 28, 2007; Revised Manuscript Received May 15, 2007

ABSTRACT: We have previously demonstrated that solution-cast films of conjugated polymers with grafted alkyl side chains comprise clearly identifiable domains ca. 10 nm in size upon solvent evaporation. Here we show that these nanodomains indeed serve as basic units for morphological development in poly(9,9-di-*n*-octyl-2,7-fluorene) (PFO) films during cold crystallization. Results of our microscopic and diffraction observations indicate that the cold crystallization process involves intradomain nucleation and growth, followed by nanodomain alignment and coalescence into fibrils in the sub-micrometer length scale via thermally activated adjustment of nanodomain orientation. An analogy with oriented aggregation (or oriented attachment−coalescence) behavior of nanocrystals of metal oxides is drawn; the relevance to recently proposed models of polymer crystallization via primary nucleation induced at the growth front is addressed.

Introduction

Previous electron microscopic observations indicated that films of conjugated polymers with grafted with flexible side chains such as poly(2,5-dialkyl-1,4-phenylenevinylene)s (PPVs)[1−3] comprise loosely adhered nanometer-sized domains formed upon solvent evaporation during film formation. Upon heat treatment, the nanodomains coalesce into string- or rodlike entities in which the conjugated backbones lie in-plane and orthogonal to the long axis. Similar morphological features have been generally observed for poly(9,9-dialkyl-2,7-fluorene)s (PFs)[4−9] and regioregular poly(3-*n*-alkyl-2,5-thiophene)s (RRPTs).[10,11] This inherent heterogeneity in the length scale of 10 nm is expected to bear relevance to morphology-dependent properties, as supported by recent X-ray scattering studies of effects of heat treatment[12] or externally applied electric field[13] on charge carrier mobility in cast films of mesomorphic poly(2-methoxy-5-(2′-ethylhexyloxy)-1,4-phenylenevinylene) (MEH−PPV).

In contrast to the mesophorphic nature MEH−PPV, poly-(9,9-di-*n*-octyl-2,7-fluorene) (PFO, chemical structure given as inset in Figure 2) exhibits well developed crystallinity[6,7,9,14] and serves as an interesting model system for investigating effects of the inherently nanoscaled heterogeneity on the development of a hierarchy of supramolecular aggregation. Previous microscopic observations indicated that melt crystallization of PFO may result in not only single crystals with lamellar thickness on the order of 10 nm (less than the contour length, suggesting folded chains) and lateral dimension on the order of 1−10 μm but also spherulites (with radius on the order of 10 μm) comprising crystalline fibrils extending radially from the sheaf-like core.[6,9] These features, much similar to crystalline assemblies in conventional polymers, are indeed surprising in view of the rigid nature of the PFO backbone: conventional wisdom would dictate absence of chain folding and predict formation
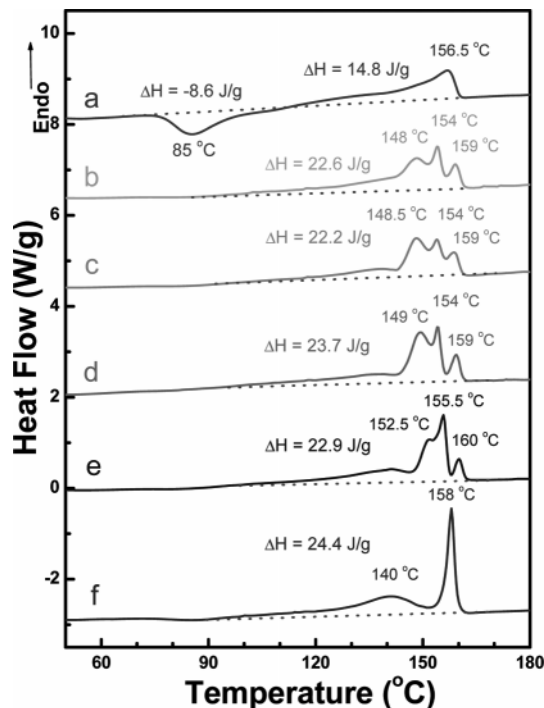

Figure 1. DSC heating traces of specimens quenched from T_{cc} at the end of cold crystallization, showing efficient crystallinity development even for the case of shortest t_{cc} of 3 min. Curve a, nematic glass; curves b−d, quenched films after cold crystallization at T_{cc} = 140 °C for t_{cc} = 3 min, 1 h, and 11 h, respectively; curve e, quenched film after cold crystallization at T_{cc} = 145 °C for t_{cc} = 18 h; curve f, quenched film after cold crystallization at T_{cc} = 150 °C for t_{cc} = 26 h.

of fringed micelle crystals.[15,16] The development of supramolecular assemblies such as lamellar single crystals and spherulites from the nanodomains is an interesting issue, for which we have previously[6,9] postulated a mechanism of attachment and coalescence of nanodomains observed earlier for nanometer-sized ordered grains[17−20] of metal oxides and surfactant-mediated silicate.[21] To verify this model, we would need morphological

† National Dong Hwa University.
‡ National Sun Yat-sen University.
§ National Synchrotron Radiation Research Center.
‖ National Tsing Hua University.

Figure 2. Grazing-incidence XRD in-depth profiles of PFO films, showing preferred formation of α crystals upon cold crystallization: curve a, nematic glass; curves b−d, quenched films after cold crystallization at T_{cc} = 140 °C for t_{cc} = 3 min, 1 h, and 11 h, respectively; curve e, quenched film after cold crystallization at T_{cc} = 145 °C for t_{cc} = 18 h; curve f, quenched film after cold crystallization at T_{cc} = 150 °C for t_{cc} = 26 h.

evidence independent of previous observations for PFO melt crystallized at an elevated temperature T_c, where nucleation is slow due to limited supercooling.

One natural approach is to examine morphological development during "cold crystallization", where glassy specimens quenched from the equilibrium melt are devitrified by reheating to the crystallization temperature (T_{cc}). This corresponds to a priori presence of densely distributed nuclei for crystallinity development and hence dramatically different morphological features due to differences in kinetic routes. In addition, we have chosen to keep the studied range of T_{cc} the same as that of T_c in the earlier melt crystallization studies to facilitate direct comparison. Here we show by microscopic and diffraction evidence that cold crystallization of PFO proceeds via nucleation (and limited growth) within the nanodomains, followed by coalescence of the crystalline nanograins into fibrils in the submicrometer length scale. In other words, nanodomains in the nematic PFO glass indeed serve as units of morphological development in the subsequent devitrification processes. Similarity with earlier observations[17−21] on oriented aggregation (or attachment−coalescence) of inorganic nanocrystals is then discussed. Relevance of present observations to recently proposed models of polymer crystallization via primary nucleation successively induced at the growth front is also addressed.

Experimental Section

The PFO sample used here was purchased from American Dye Source, Quebec, Canada (cat. no. ADS129BE). The weight-average molecular mass (M_w) was 65 kDa, and polydispersity index PDI = 2.6 as determined via GPC using polystyrene standards. Since small-angle light scattering results of Grell et al.[22] suggested a correction factor of $(2.7)^{-1}$ = 0.37, the true M_w value is estimated to be 24 kDa.

Transmission electron microscopic (TEM) studies were performed using a JEOL 3010 instrument under an acceleration voltage of 200 kV, at which the combined factor of wavelength and camera length has been carefully calibrated using (111), (200), (220), and (311) reflections from vapor-deposited Al thin film. Field-emission scanning electron microscopic (FE-SEM) observations were made by use of a JEOL JSM-6700F instrument operated at an accelerating voltage of 10 kV. For the grazing-incidence X-ray diffraction (GI-XRD) study, a Bede D1 HR-XRD diffractometer (equipped with a copper target for Kα line of wavelength 0.154 nm, polycapillary collimator/lens, and parabolic multilayer mirrors) was used under

a step-scan rate of 0.05° per 5 s in the scattering angle range of 3°−37°. Full range calibration of the scattering angle was made using both silicon and silver behenate standards.

Films were drop-cast from dilute (ca. 0.1% w/v) solutions of PFO in toluene on inclined glass substrates. The as-cast films were routinely heat-treated via a brief 1 min residence at 200 °C or above (equilibrium melting temperature of PFO is recently determined as $T_m° \approx$ 180 °C)[23] to eliminate previous processing history, followed by quenching into ice water to obtain films of nematic glass. The nematic films were then "cold-crystallized" by rapidly heated to and maintained at an elevated temperature (T_{cc}, in the range of 140−150 °C) significantly above its glass transition temperature (T_g) but below the melting temperature (T_m) for different periods of time (t_{cc}, up to 26 h). Because of preferred nucleation of the α crystalline phase[4,5] at low temperatures, this cold crystallization procedure always results in dominance of α crystals. All heat treatments were made by use of a Linkman THMS-600 high-temperature stage (connected to a TMS-91 temperature controller) under a protective nitrogen atmosphere. TEM specimens were detached from the glass substrate using a dilute HF solution. These specimens were then vapor-deposited with carbon prior to TEM examinations.

For comparison with microscopic and diffraction results, differential scanning calorimetric (DSC) measurements over specimens of the same thermal history were taken by use of a Perkin- Elmer Diamond instrument (routinely calibrated using indium standard) at a heating rate of 10 °C/min under a stream of nitrogen atmosphere. Real-time small-angle X-ray scattering (SAXS) measurements on a liquid-nitrogen-quenched (from nematic melt state) PFO specimen at a heating rate of 10 °C/min were performed at the BL17B3 beamline of the National Synchrotron Radiation Research Center (NSRRC). The sample was inserted between Kapton films, sealed with Al pan/cap (with circular holes 4 mm in diameter punctured at the center to allow for incidence of the X-ray beam) for good thermal contact, and placed in a Mettler Toledo FP84 DSC cell, which serves as a temperature-programmed specimen holder with an circular opening 2 mm in diameter allowing the X-ray beam to pass through. The incident beam (0.5 mm in diameter) was monochromated to 8 keV (wavelength λ = 1.55 Å) by use of a Si (111) double-crystal monochromator and collimated by a set of slits and two sets of Ta pinholes. With a sample-to-detector distance of 2715.7 mm and a beam stop of 6 mm diameter, we collected SAXS data using a 2-D multiwire proportional counter. All the SAXS data were corrected for sample transmission, background, and detector sensitivity. The scattering vector, $q \equiv 4\pi\lambda^{-1} \sin(\theta/2)$ where θ is the scattering angle, was calibrated by use of silver behenate. A polyethylene standard was used for the calibration of the absolute intensity $I(q)$. On the basis of a photon flux of 10^9 photons s^{-1} at 8 keV, a minimum time resolution of 1 min is required for data acquisition.

Results

Crystallinity Development upon Cold Crystallization. Given in Figure 1 are heating traces at 10 °C/min of as-quenched (directly from the equilibrium melt) and cold-crystallized specimens. The heating trace (curve a in Figure 1) of the as-quenched specimen exhibits a clear cold crystallization exotherm (7 J/g) in the range of 70−110 °C (slightly above its T_g of 62 °C),[8] followed by a broad melting endotherm (implying significant premelting, reorganization, and remelting) up to 157 °C, with endothermic heat of ca. 15 J/g. Within the error of DSC measurements, we conclude that there was ca. 10% crystallinity in the as-quenched specimen on the basis of an estimated heat of melting ΔH_m = 73 J/g for perfectly crystalline PFO.[23] It is then interesting to note that this nonnegligible crystallinity in the as-quenched specimen, however, results in no discernible peaks in the corresponding GI-XRD profile (top curve in Figure 2). Hence, the crystallites must be of very small size that their contributions to diffraction intensities are

broadened and smeared into the background, whereas the number of crystallites per unit volume must be high to match such limited yet significant crystallinity. The densely distributed crystallites generated at low temperatures during the quenching process then serve as nuclei for later crystal growth, as delineated below.

Allowing for a short period (3 min) of cold crystallization at $T_{cc} = 140$ °C, significant increase in crystallinity was observed (curve b in Figure 1), and no cold crystallization endotherm in the low-temperature range was observed. The melting endotherm resolved into three peaks, located at $T_{m1} = 148$ °C, $T_{m2} = 154$ °C, and $T_{m3} = 159$ °C. Among them, T_{m1} corresponds to initial melting of the cold-crystallized crystals and T_{m3} to final melting of well-perfected crystals during heating. The origin of T_{m2} is less clear, but we tentatively attribute it to melting of reorganized crystals of moderate perfection (as compared to those of T_{m3}). In the case of highest T_{cc} of 150 °C, the three peaks merge into a single endotherm located at 158 °C (i.e., 8 °C above T_{cc}). In all cases, broad endothermic contributions below T_{cc} are attributable to minor crystallinity developed during quenching or reheating.

More importantly, the total endothermic heat in the case of 3 min cold crystallization at 140 °C (curve b in Figure 1) corresponds to 23 J/g, which translates to ca. 30% crystallinity. Within this short period of 3 min, the crystallization process is largely complete, as further increases in t_{cc} up to 11 h resulted in insignificant changes in crystallinity and only slight increases of T_{m1} to 149 °C (curves b−d). This efficient process of cold crystallization at an elevated temperature distant from T_g (such that the controlling factor of crystallization kinetics is nucleation rather than growth) justifies our interpretation that existing crystallites (formed during quenching, that are of small size and densely distributed in space) within the as-quenched specimens serve as nuclei for the subsequent cold crystallization process.

In support of this scenario are real-time SAXS profiles (Figure 3) of an as-quenched PFO specimen upon heating at 10 °C from the glassy state, which corresponds to curve a in Figure 1 up to 145 °C. At temperatures below 70 °C (cf. Figure 2a), the SAXS intensity profile exhibited monotonic decay with increasing q and was insensitive to changes in temperature. Significant increases in intensity with increasing temperature was observed in the high-q region as the temperature reaches 80 °C, where the corresponding DSC trace (curve a in Figure 1) exhibits the start of a cold crystallization exotherm. The cold crystallization process here likely involves both formation of new nuclei and growth of existing nuclei as the intensity increase spans the entire high-q (>0.2 nm^{-1}) range.

As the temperature exceeded 120 °C (which corresponds to the onset of the broad melting endotherm in curve a of Figure 1) up to the upper temperature of 145 °C, the SAXS profile the scattered intensity continues to increase only for $q < 0.25$ nm^{-1}; concurrently, the scattered intensity for $q > 0.25$ nm^{-1} decreases with increasing temperature. The integrated intensity in the full q range up to 0.2 nm^{-1} decreases only moderately (as compared to the profile at 120 °C which represents the end of the cold crystallization exotherm), consistent with the limited area under the melting endotherm up to 145 °C in curve a of Figure 1. This corresponds well to the melting−reorganization process in our discussion of DSC results. It is clear that the rate of the reorganization process is fast, effective even at the fairly high heating rate of 10 °C/min adopted here. More interestingly, the observation that the subsequent isothermal treatment (up to 10 min) at this maximum temperature of 145 °C results in little change in the SAXS profile (cf. Figure 3b). In other words, the

reorganization process observed here is not only thermally activated but also "instantaneously" completed (within the present time resolution of 1 min); it is hence characteristically different from the well-recognized and comparatively slow process of lamellar thickening upon long-term annealing, which is still in its incubation period within the experimental time frame here. Although both processes are consistent with the intrinsic metastability of polymer lamellar crystals, there appear to be significant differences in the kinetic paths. This deserves further experimental scrutiny in the future.

We now return to GI-XRD in-depth profiles in Figure 2. While the as-quenched film (curve a) indeed showed glasslike features, the emergence of several weak ($hk0$) reflections was observed upon extended cold crystallization at 140 °C (curves b−d). Values of the coherent length, l_c, as calculated from width of the most prominent (200) reflection, are 37, 44, and 45 nm for $t_{cc} = 3$ min, 1 h, and 11 h, respectively, suggesting quickly improved but then plateaued positional order. Further increases in T_{cc} and t_{cc} to 145 °C/18 h (curve e) or 150 °C/26 h (curve f) resulted in generally better resolved ($hk0$) reflections; l_c values along the [200] direction (42 and 47 nm, respectively) remained largely comparable to the plateau value of $T_{cc} = 140$ °C, implying generally limited development of positional order along the crystallographic a-axis. In contrast, the l_c value along the [220] direction increased from 39 to 62 nm in the two high-T_{cc} cases, suggesting continued positional ordering along the crystallographic b-axis that corresponds to the fibrillar axis in melt-crystallized PFO axialites or spherulites.[9]

Nanograins in Cold-Crystallized PFO. Although crystallized within the same temperature range adopted in previous melt crystallization studies where single crystals and axialites were observed, morphological features in the present case of cold crystallization are dramatically different. Given in Figure 4 are secondary electron images (SEIs) of the PFO thin films before and after cold crystallization. The as-quenched film is characterized by nodules ca. 10 nm in size (Figure 4a), embedded in a matrix of less prominent nanodomains. A crack extending from left to central regions of view is observed to propagate around (rather than passing through) the nodules, much like fractographic features in filled composites.[24] This implies stress concentration and hence rigid nodules as compared to the soft matrix of nanodomains, which is consistent with our contention of existing nuclei in the as-quenched specimens. Upon cold crystallization (Figure 4b), the nodular features are more clearly identifiable, which appear to become aligned into strings of nanograins with increasing t_{cc} or T_{cc} (Figure 4c−e).

More direct evidence for nanograins to align themselves upon prolonged cold crystallization at an elevated temperature come from TEM observations. Consistent with SEM results, bright-field images (BFIs) given in Figure 5 indicate general presence of nanograins. More importantly, the corresponding selected-area electron diffraction (SAED) pattern (taken from central region of the view) changes from rings comprising identifiably discrete spots for short-term crystallized (Figure 5a) to arcs of finite azimuthal spans in long-term crystallized (11 h, Figure 5b) specimens. Upon increases in crystallization temperature and time, the azimuthal spans of all reflection arcs decrease further, resulting in fiberlike patterns (Figure 5c,d). Note that the observed reflections (as indexed in the SEAD patterns) indicate the tendency toward preferred in-plane orientation of the crystallographic c-axis (i.e., the PFO backbone axis), whereas a- and b-axes remain more or less randomly oriented. We note further that, as the as-quenched or short-term crystallized specimens do not exhibit clear nanograin orientation in the
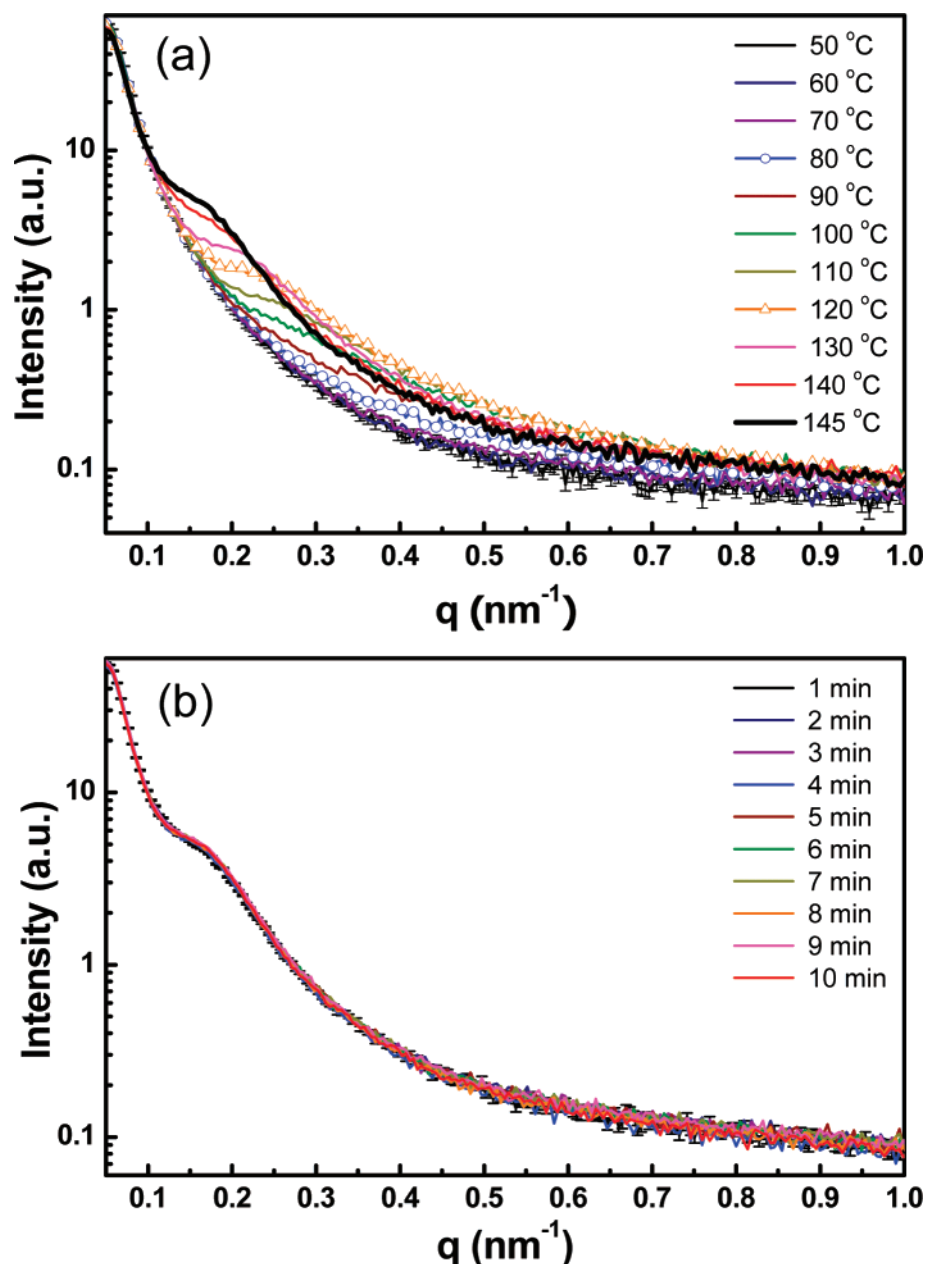
Figure 3. Synchrotron radiation SAXS profiles obtained during heating of an as-quenched PFO specimen (a) upon heating at 10 °C/min from ambient to 145 °C and (b) during subsequent isothermal holding at 145 °C up to 10 min. Significant increases in scattering intensity in the high-q range was observed when heated above T_g (≈ 60 °C), showing onset of cold crystallization near 80 °C that results in crystallites of small and broadly distributed size in the range of 10−25 nm. The initial stage of cold crystallization is largely completed near 120 °C; further increases in temperature result in increased intensity in the low-q region with concomitant decrease in intensity in the high-q range, signifying increased crystallite size up to ca. 35 nm with increasing temperature. Subsequent isothermal heat treatment at 145 °C resulted in little changes in the SAXS profile, indicating that the cold crystallization process is intrinsically rapid and the absence of discernible lamellar thickening/reorganization within this 10 min period of isothermal annealing.

spatial range of 0.3 μm (i.e., the adopted aperture size), the observed nanograin orientation occurs only after crystallinity development. In other words, the liquid crystalline nature in the melt state is not directly related to the observed nanograin orientation in the later stage of morphological development.

Discussion

Attachment−Coalescence of Nanograins. Formation of nanograins as primitive form of crystals is not limited to the present case of PFO or its homologues. Reported examples include nanocrystals of metal oxides[17−20] and surfactant-mediated mesoporous silicate.[21] Oriented aggregation (as termed by Penn et al.)[17,18] or attachment−coalescence (as termed by Shen et al.)[19−21] of crystalline nanoclusters was suggested as

the growth mechanism of nanocrystallites on the basis of high-resolution TEM observations of a significant number of dislocations that should otherwise be scarce in view of the limited size of nanocrystallites. The key feature in this mechanism of crystallization is the simultaneous presence or concurrent emergence (implying generally far-from-equilibrium conditions) of a fairly large number of crystalline nanoclusters that serve as units of morphological development; this is satisfied in the present case of cold crystallization of PFO. The process of (perfectly or imperfectly) oriented attachment and coalescence is certainly plausible if the nanoclusters are suspended in a fluid medium of low viscosity or under vacuum, but this is not a strict prerequisite. Previous TEM observations indicated rotation of nanograins of nickel oxides embedded in $NiAl_2O_4$[25] or
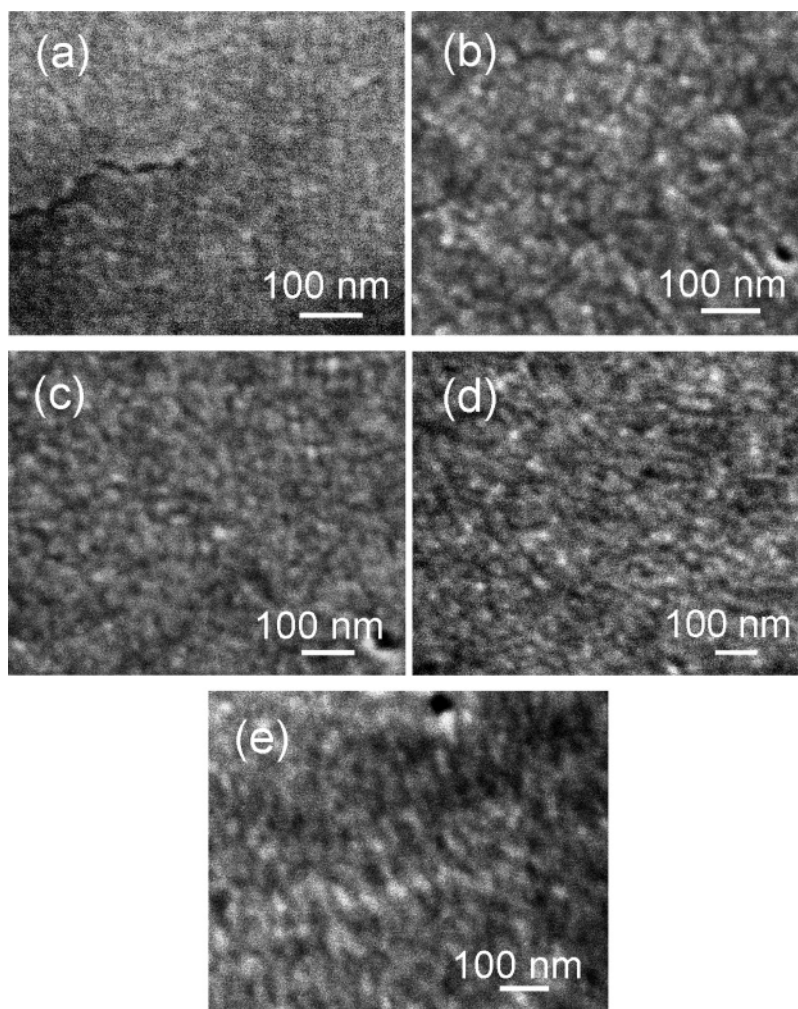
Figure 4. Representative SEIs of cold-crystallized PFO films, suggesting local alignment of nanograins with increasing t_{cc} or T_{cc}: (a) nematic glass; (b, c) quenched after t_{cc} = 3 min and 1 h, respectively; at T_{cc} = 140 °C; (d) quenched after t_{cc} = 18 h at T_{cc} = 145 °C; (e) quenched after t_{cc} = 26 h at T_{cc} = 150 °C.

zirconia[26] matrix upon adequate thermal activation at an elevated temperature. The key issue in the attachment−coalescence process of confined nanocrystallites in 3D is their ability to rotate: since the rotational kinetic energy of a nearly spherical particle of radius r scales as r^5 whereas the translational counterpart scales as r^3, rotational motion of small particles is increasingly easier (as compared to translation) to be thermally activated as the particle size decreases to the nanometer length scale. The present case of long-term cold crystallization of PFO serves as an independent demonstration for feasibility of such a process; a relatively high T_{cc} for adequate thermal activation is understandably required.

The observation of the tendency of the crystallographic c-axis to lie in-plane whereas a- and b-axes remain randomly oriented deserves further comments. We note that this is in contrast to the preferred in-plane alignment of b- and c-axes in axialites or spherulites developed during melt crystallization.[9] It signifies the concurrent orientation adjustment of neighboring nanograins in different locations during cold crystallization; in melt crystallization, the attachment−coalescence process occurs only at the crystal growth front, resulting in more coherent orientation (and preferred growth) along the b-axis. This orientation process during isothermal cold crystallization cannot be attributable to Oswald ripening, as Oswald ripening involves growth of large particles at the expense of smaller particles through molecular migration/reorganization, which would result in changes in

morphological features. Our electron micrographs indicate clear contrast for nanograins; their size remained little changed with time.

Relevance to Melt Crystallization. Present results indicate rotation−attachment−coalescence of nanograins as the dominant mode of morphological development in cold-crystallized PFO at the same temperature range of previous melt crystallization studies. We now concentrate on the issue that whether this process contributes significantly to the melt crystallization of PFO. We note first that the melt crystallization temperature range of 140−150 °C in previous studies corresponds to supercoolings $\Delta T \equiv T_m° - T_c = 30-40$ °C, which are significantly away from equilibrium as characteristic of melt crystallization of polymers in general. In contrast to the present case of cold crystallization of PFO where nanocrystallites are inherently dominating, the melt crystallization counterpart is characteristically low in the rate of primary nucleation such that single crystals, axialites, and eventually spherulites are dominant supramolecular aggregates observed; however, nanometer-sized grainy features persist under high magnifications.[6,9] Nanodomain features inherent to solution-cast PFO films[8] could have left some traces of their prior existence upon melt crystallization, but one would nevertheless expect smoothening or smearing of the grainy features if the Hoffman−Lauritzen model of stem-by-stem attachment (followed by spreading) at the crystal front[27,28] is adopted. The clear presence of nanograins in the
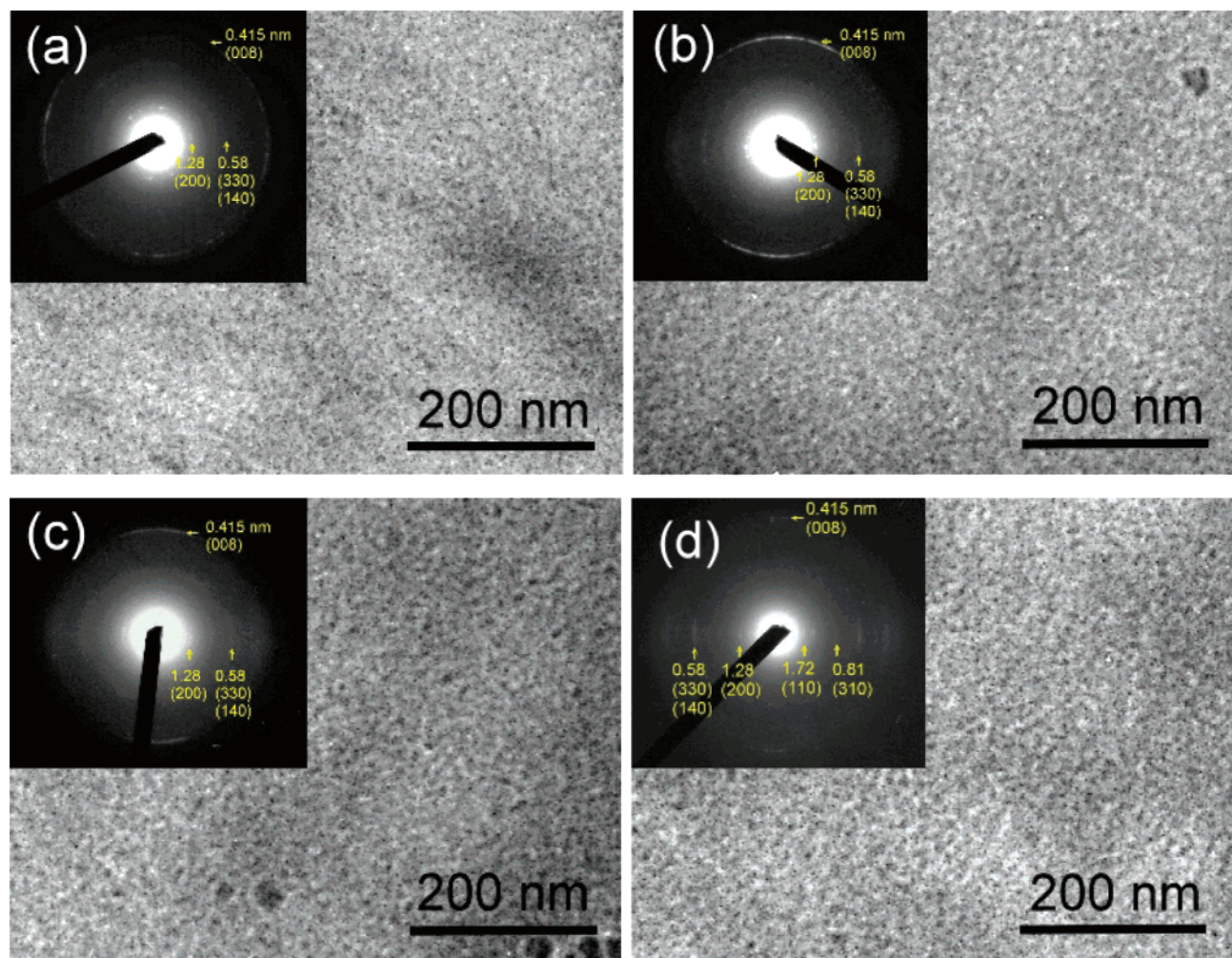
Figure 5. Representative BFIs and corresponding SAED patterns (rotated to let the c^*-axis coincide with the meridian when applicable, taken from central region of BFI with an aperture size of 0.3 μm) of PFO films, indicating preferred formation of nanograins and their alignment with increasing t_{cc} or T_{cc}: (a, b) quenched upon cold-crystallization at T_{cc} = 140 °C for t_{cc} = 3 min and 11 h, respectively; (c) quenched upon cold crystallization at T_{cc} = 145 °C for t_{cc} = 18 h, and (d) quenched upon cold crystallization at T_{cc} = 150 °C for t_{cc} = 26 h.

melt-crystallized supramolecular aggregates of PFO is more easily understandable if primary nuclei can be induced (say, by partial alignment of chain segments due to wall effects from the approaching growth front) within nanodomains at (or in close vicinity of) the growth front. Subsequent processes of attachment and coalescence, as demonstrated feasible for cold crystallization of PFO in the same temperature range, may then explain the retained nanograin features observed in melt-crystallized supramolecular aggregates. In support of this model, we have observed a clear dependence of axialitic or spherulitic growth rate on orientation of the nematic melt matrix.[9]

Interestingly, a related model of melt crystallization for conventional polymers has been enthusiastically advocated by Strobl[29] in recent years, in spite of opposing argument given by Lotz[30] on the basis of packing of helical chains of opposite chiral senses. The key process in Stobl's model is the induced formation of mesomorphic nodules at the crystal growth front. Similar features of induced primary ("intramolecular") nucleation have also been indicated by recent results of molecular dynamics simulations from Muthukumar et al.[31−35] and Frenkel et al.[36,37] There are also models where the growth front is not specifically incorporated into (but certainly not excluded from) consideration. Allegra[38,39] recently modified his earlier bundle theory[40] to better explain fractionation effects upon melt crystallization, for which Wunderlich[15] had hypothesized (albeit without clear delineation of the detailed mechanism involved)

"molecular" nucleation decades ago. As summarized in a recent review,[41] an extensive series of studies (first on cold crystallization and later on extended to melt crystallization of conventional polymers) of Kaji et al. have led to a general scheme describing various paths of structural development in the initial stage of polymer crystallization, in which formation of nematic- and smectic-like mesophases are postulated as intermediates toward the final crystalline state. All these models suggest, in one way or another, some intermediate ordering either generally in the melt or specifically at the crystal front. By and large, in the forming is the view that enhanced primary nucleation at the growth front is likely an alternative route not accounted for by the classical Hoffman−Lauritzen kinetic model of polymer crystallization. Our observations of nanograin features of melt- and cold-crystallized PFO appears consistent with this line of thought. In Strobl's model, an adsorbed layer of mesomorphic metastable phase at the crystal growth front is postulated.[29] For the present case of PFO, the melt state is, by its nature, mesomorphic (or, more specifically, nematic in terms of optical texture)[8] and hence consistent with Strobl's hypothesis. Nevertheless, for general polymers, it appears that the (purely geometric) wall effects from the approaching crystal growth front could be adequate to induce chain alignment and hence primary nucleation; the postulated presence of a separate phase of mesomorphic order in general awaits more thorough experimental confirmation.

As a final remark, we note that an indirect evidence in support of the present model of morphological development in terms of Brownian rotation, oriented attachment, and coalescence of nanograins comes from the observation of the comparatively short lifetime (in the order of a few seconds) for SAED patterns of melt- and cold-crystallized PFO specimens under electron beam. For conventional polymer crystals (such as polyethylene or syndiotactic polystyrene), the corresponding lifetime under similar operating conditions is typically an order of magnitude longer. This implies exceedingly high density of defects in PFO crystals, characteristic of aggregated nanocrystals after oriented attachment and coalescence.

References and Notes

(1) Chen, S. H.; Su, A. C.; Chou, H. L.; Peng, K. Y.; Chen, S. A. *Macromolecules* **2004**, *37*, 167.
(2) Chen, S. H.; Su, A. C.; Han, S. R.; Chen, S. A.; Lee, Y. Z. *Macromolecules* **2004**, *37*, 181.
(3) Chen, S. H.; Su, C. H.; Su, A. C.; Chen, S. A. *J. Phys. Chem. B* **2004**, *108*, 8855.
(4) Teetsov, J. A.; Vanden Bout, D. A. *J. Am. Chem. Soc.* **2001**, *123*, 3605.
(5) Teetsov, J.; Vanden, Bout, D. A. *Langmuir* **2002**, *18*, 897.
(6) Chen, S. H.; Chou, H. L.; Su, A. C.; Chen, S. A. *Macromolecules* **2004**, *37*, 6833.
(7) Chen, S. H.; Su, A. C.; Su, C. H.; Chen, S. A. *Macromolecules* **2005**, *38*, 379.
(8) Chen, S. H.; Su, A. C.; Chen, S. A. *J. Phys. Chem. B* **2005**, *109*, 10067.
(9) Chen, S. H.; Su, A. C.; Chen, S. A. *Macromolecules* **2006**, *39*, 9143.
(10) Kim, D. H.; Park, Y. D.; Jang, Y.; Yang, H.; Kim, Y. H.; Han, J. I.; Moon, D. G.; Park, S.; Chang, T.; Chang, C.; Joo, M.; Ryu, C. Y.; Cho, K. *Adv. Funct. Mater.* **2005**, *15*, 77.
(11) Kline, R. J.; McGehee, M. D.; Kadnikova, E. N.; Liu, J.; Fréchet, J. M. J.; Toney, M. F. *Macromolecules* **2005**, *38*, 3312.
(12) Inigo, A. R.; Chang, C. C.; Fann, W.; White, J. D.; Huang, Y. S.; Jeng, U. S.; Sheu, H. S.; Peng, K. Y.; Chen, S. A. *Adv. Mater.* **2005**, *17*, 1835.
(13) Jeng, U.; Hsu, C. H.; Sheu, H. S.; Lee, H. Y.; A. R. Inigo, A. R.; H. C. Chiu, H. C.; Fann, W. S.; Chen, S. H.; Su, A. C.; Lin, T. L.; Peng, K. Y.; Chen, S. A. *Macromolecules* **2005**, *38*, 6566.
(14) Grell, M.; Bradley, D. D. C.; Ungar, G.; Hill, J.; Whitehead, K. S. *Macromolecules* **1999**, *32*, 5810.
(15) Wunderlich, B. *Macromolecular Physics*; Academic Press: New York, 1976; Vol. 2, Chapter 5.
(16) Sperling, L. H. *Introduction to Physical Polymer Science*, 3rd ed.; Wiley: New York, 2001; Chapter 6.
(17) Penn, R. L.; Banfield, J. F. *Science* **1998**, *281*, 969.
(18) Penn, R. L. *J. Phys. Chem. B* **2004**, *108*, 12707.
(19) Shen, P.; Lee, W. H. *Nano Lett.* **2001**, *1*, 707.
(20) Tsai, M. H.; Chen, S. Y.; Shen, P. *Nano Lett.* **2004**, *4*, 1197.
(21) Shen, P.; Fahn, Y. Y.; Su, A. C. *Nano Lett.* **2001**, *1*, 299.
(22) Grell, M.; Bradley, D. D. C.; Long, X.; Chamberlain, T.; Inbasekaran, M.; Woo, E. P.; Soliman, M. *Acta Polym.* **1998**, *49*, 439.
(23) Chen, S. H.; Su, C. H.; Su, A. C.; Sun, Y. S.; Jeng, U.; Chen, S. A. *J. Appl. Crystallogr.* **2007**, *40*, s573.
(24) Hull, D.; Clyne, T. W. *An Introduction to Composite Materials*, 2nd ed.; Cambridge University Press: Cambridge, 1996; Chapter 8.
(25) Wang, S. R.; Shen, P. *Mater. Sci. Eng., A* **1998**, *251*, 106.
(26) Lin, K. T.; Shen, P. *Mater. Sci. Eng., A* **1999**, *270*, 125.
(27) Hoffman, J. D.; Davis, G. T.; Lauritzen, J. I. In *Treatise in Solid State Chemistry*; Hannay, N. B., Ed.; Plenum: New York, 1976.
(28) Hoffman, J. D.; Miller, J. D.; Marand, H.; Roitman, D. B. *Macromolecules* **1992**, *25*, 2221.
(29) Strobl, G. *Eur. Phys. J. E* **2000**, *3*, 165 and references cited therein.
(30) Lotz, B. *Eur. Phys. J. E* **2000**, *3*, 185 and references cited therein.
(31) Liu, C.; Muthukumar, M. *J. Chem. Phys.* **1998**, *109*, 2536.
(32) Muthukumar, M.; Welch, P. *Polymer* **2000**, *41*, 8833.
(33) Welch, P.; Muthukumar, M. *Phys. Rev. Lett.* **2001**, *87*, 218302.
(34) Dukovski, I.; Muthukumar, M. *J. Chem. Phys.* **2003**, *118*, 6648.
(35) Muthukumar, M. *Philos. Trans. R. Soc. London A* **2003**, *361*, 539.
(36) Hu, W.; Frenkel, D.; Vincent, B. F.; Mathot, V. B. F. *Macromolecules* **2003**, *36*, 549.
(37) Hu, W.; Frenkel, D.; Vincent, B. F.; Mathot, V. B. F. *Macromolecules* **2003**, *36*, 8178.
(38) Allegra, G.; Meille, S. V. *Phys. Chem. Chem. Phys.* **1999**, *1*, 5179.
(39) Allegra, G.; Meille, S. V. *Adv. Polym. Sci.* **2005**, *191*, 87.
(40) Allegra, G. *J. Chem. Phys.* **1977**, *66*, 5453.
(41) Kaji, K.; Nishida, K.; Kanaya, T.; Matsuba, G.; Konishi, T.; Imai, M. *Adv. Polym. Sci.* **2005**, *191*, 187 and references cited therein.